LETTERS

Soft X-ray microscopy at a spatial resolution better than 15 nm

Weilun Chao[1,2], Bruce D. Harteneck[1], J. Alexander Liddle[1], Erik H. Anderson[1] & David T. Attwood[1,2]

Analytical tools that have spatial resolution at the nanometre scale are indispensable for the life and physical sciences. It is desirable that these tools also permit elemental and chemical identification on a scale of 10 nm or less, with large penetration depths. A variety of techniques[1–7] in X-ray imaging are currently being developed that may provide these combined capabilities. Here we report the achievement of sub-15-nm spatial resolution with a soft X-ray microscope—and a clear path to below 10 nm—using an overlay technique for zone plate fabrication. The microscope covers a spectral range from a photon energy of 250 eV (~5 nm wavelength) to 1.8 keV (~0.7 nm), so that primary K and L atomic resonances of elements such as C, N, O, Al, Ti, Fe, Co and Ni can be probed. This X-ray microscopy technique is therefore suitable for a wide range of studies: biological imaging in the water window[8,9]; studies of wet environmental samples[10,11]; studies of magnetic nanostructures with both elemental and spin-orbit sensitivity[13–14]; studies that require viewing through thin windows, coatings or substrates (such as buried electronic devices in a silicon chip[15]); and three-dimensional imaging of cryogenically fixed biological cells[9,16].

The microscope XM-1 at the Advanced Light Source (ALS) in Berkeley[17] is schematically shown in Fig. 1. The microscope type is similar to that pioneered by the Göttingen/BESSY group (ref. 18, and references therein). A 'micro' zone plate (MZP) projects a full-field image to an X-ray-sensitive CCD (charge-coupled device), typically in one or a few seconds, often with several hundred images per day. The field of view is typically 10 μm, corresponding to a magnification of 2,500. The condenser zone plate (CZP), with a central stop, serves two purposes in that it provides partially coherent hollow-cone illumination[2], and, in combination with a pinhole, serves as the monochromator. Monochromatic radiation of $\lambda/\Delta\lambda = 500$ is used. Both zone plates are fabricated in-house, using electron beam lithography[19].

The spatial resolution of a zone plate based microscope is equal to $k_1\lambda/NA_{MZP}$ where λ is the wavelength, NA_{MZP} is the numerical aperture of the MZP, and k_1 is an illumination dependent constant, which ranges from 0.3 to 0.61. For a zone plate lens used at high magnification, $NA_{MZP} = \lambda/2\Delta r_{MZP}$ where Δr_{MZP} is the outermost (smallest) zone width of the MZP[20]. For the partially coherent illumination[21,22] used here, $k_1 \approx 0.4$ and thus the theoretical resolution is $0.8\Delta_{MZP}$, as calculated using the SPLAT computer program[23] (a two-dimensional scalar diffraction code, which evaluates partially coherent imaging). In previous results with a $\Delta r_{MZP} = 25$ nm zone plate, we reported[2] an unambiguous spatial resolution of 20 nm. Here we describe the use of an overlay nanofabrication technique that allows us to fabricate zone plates with finer outer zone widths, to $\Delta r_{MZP} = 15$ nm, and to achieve a spatial resolution of below 15 nm, with clear potential for further extension.

This technique overcomes nanofabrication limits due to electron beam broadening in high feature density patterning. Beam broadening results from electron scattering within the recording medium (resist), leading to a loss of image contrast and thus resolvability for dense features. This effect is reduced by writing only semi-isolated features. Here the dense zone plate pattern is subdivided into two less dense, complementary patterns, which are fabricated separately and then overlaid with high accuracy to yield the desired pattern. The overlay technique allows us to achieve pattern densities several times higher than would otherwise be possible. The required placement accuracy for zone plates is typically one-third the smallest feature size—thus about 5 nm for the optic reported here with a 15 nm outer zone width. As described below, the zone placement accuracy achieved here is better than 2 nm across the two-dimensional field, leaving significant room for further zone plate advances. Note that this high placement accuracy overlay technique permits the achievement of smaller zones without incurring the low diffraction efficiency inherent to photon sieves[3], where pinhole distribution must meet the same tight placement constraints.

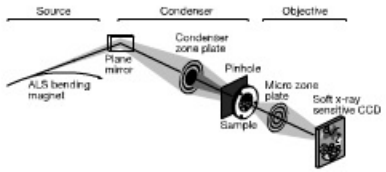

Figure 1 | A diagram of the soft X-ray microscope XM-1. The microscope uses a micro zone plate to project a full field image onto a CCD camera that is sensitive to soft X-rays. Partially coherent, hollow-cone illumination of the sample is provided by a condenser zone plate. A central stop and a pinhole provide monochromatization.

Figure 2 | An illustration of the overlay nanofabrication technique for micro zone plate fabrication. The zone plate is composed of even-numbered opaque zones (black and grey) and odd-numbered transparent zones (white). Set I (black), containing zones 2, 6, 10 …, and its complement, set II (grey), are fabricated sequentially to form the desired overlaid micro zone plate.

[1]Center for X-ray Optics, Lawrence Berkeley National Laboratory, 1 Cyclotron Road, MS 2-400, [2]Department of Electrical Engineering and Computer Sciences, University of California, Berkeley, California 94720, USA.

For the 15 nm zone plates reported here, the odd-numbered zones are transparent, while the even-numbered are opaque. The even-numbered zones are subdivided into two complementary sets: set I, containing zones 2, 6, 10…, and set II, containing zones 4, 8, 12,…, as illustrated in Fig. 2. The nanofabrication process will be described in further detail elsewhere (W.C., J.A.L., E.A. and B.H., manuscript in preparation). The complete zone plate fabrication was conducted in-house, using our vector-scan electron beam lithography tool, the Nanowriter[19], which has a 6.5 nm diameter (full-width at half-maximum) 100 keV electron beam, and excellent zone placement accuracy. The latter property is achieved by a combination of nanometre beam position control, accurate distortion calibration, and the use of a pattern generator specially designed for curved shapes[24]. The resist, polymethyl methacrylate (PMMA), was used for pattern recording, while all opaque zones were formed by gold plating in a multistep process[19] for reasonable zone plate efficiency, in the operating spectral range from 250 eV to 1.8 keV.

High alignment accuracy is the key to the success of our technique. Before exposure of the zone plate patterns, the Nanowriter's beam deflection was calibrated, using an in-house alignment algorithm[25], to the pre-fabricated alignment marks on the resist-coated wafer. This technique greatly reduces systematic zone placement errors, allowing us to consistently achieve a subpixel placement accuracy of 1.7 nm (1 s.d.). In Fig. 3, a scanning electron micrograph shows the outer zone region of a 15 nm zone plate, revealing near perfect alignment of the opaque zones. The gold zones contain small gaps at various positions, and have widths larger than desired, thus reducing efficiency in these early results. We expect to improve these in the future. The gold plated zones are 80 nm thick, as needed for opacity and thus efficiency, giving an aspect ratio of 5:1. The calculated diffraction efficiency to first order is 6%. Transmission of the substrate and plating base, which support the zone plate, is 70%, so the expected zone plate efficiency is 4%. This is typical of early state-of-the-art zone plates, and is consistent with our observed exposure time.

Using this zone plate, the microscope was used to image several patterns, including 15.1 nm and 19.5 nm half-period test objects at 1.52 nm wavelength ($h\nu = 815$ eV), with a magnification of 7,600. For optimal signal to noise ratio, the exposure time was 62 s, with 10^4 counts per pixel in the 2,048 × 2,048 pixel array CCD detector. This exposure time is about 30 times longer than would be used in normal imaging. In order to minimize the effect of photon and electronic noise and CCD pixel size on the image resolution, we chose to collect about 8 times more photons per pixel than is typical, for improved statistics (10^4 compared to 10^3 photons per pixel), and we used 4 times more pixels than is typical for high spatial resolution recording at the same magnification. That is, we used a 2,048 × 2,048 pixel CCD (1.6 nm × 1.6 nm equivalent pixel size) rather than a 1,024 × 1,024 CCD (3.2 nm × 3.2 nm effective pixel size). For the imaging experiments here, the microscope configuration (Fig. 1) used is as follows. MZP: $\Delta r_{MZP} = 15$ nm, 500 zones, 30 μm diameter; CZP: $\Delta r_{CZP} = 40$ nm, 56,250 zones, 9.0 mm outer diameter, 5 mm diameter central stop; pinhole, 14 μm. The degree of partial coherence[2,21,22], σ, is 0.38. The test objects used for these resolution studies were Cr/Si multilayer coatings[20] in cross-section; they were fabricated in-house, using magnetron sputtering and conventional transmission electron microscopy sample preparation techniques[26].

Images obtained with the two zone plate lenses, having outer zone widths of 25 nm and 15 nm, are shown in Fig. 4. The two images on the left, Fig. 4a and c, were obtained with the 25 nm zone plate, at a wavelength of 2.07 nm (600 eV). This photon energy is just above the

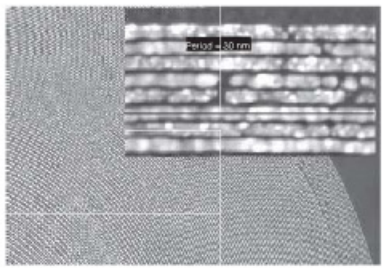

Figure 3 | Scanning electron micrograph of a zone plate with 15 nm outermost zone. Shown in the inset is a more detailed view of the outermost zones. The zonal period, as indicated by the two black lines, is measured to be 30 nm. The zone placement accuracy is measured to be 1.7 nm.

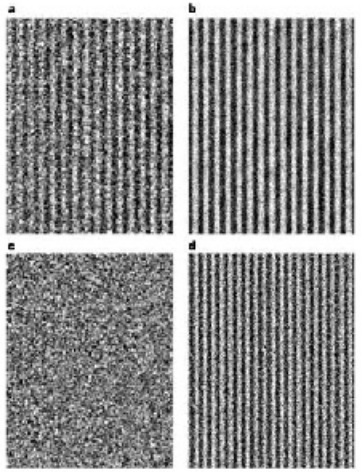

Figure 4 | Soft X-ray images of 15.1 nm and 19.5 nm half-period test objects, as formed with zone plates having outer zone widths of 25 nm and 15 nm. The test objects consist of Cr/Si multilayers, with 15.1 nm and 19.5 nm half-periods, respectively. Significant improvements are noted between the images obtained with the new 15 nm zone plate, as compared to earlier results obtained with the 25 nm zone plate. This is particularly evident for the 15 nm half-period images, for which the earlier result shows no modulation, whereas the image obtained with the 15 nm zone plate shows excellent modulation. **a**, Image of 19.5 nm half-period test object obtained previously with a 25 nm zone plate. **b**, Image of 19.5 nm half-period object with the 15 nm zone plate. **c**, Image of 15.1 nm half-period with the previous 25 nm zone plate. **d**, Image of 15.1 nm half-period with the 15 nm zone plate. Images **a** and **c** were obtained at a wavelength of 2.07 nm (600 eV photon energy); **b** and **d** were obtained at a wavelength of 1.52 nm (815 eV). The equivalent object plane pixel size for images **a** and **c** is 4.3 nm; the size for **b** and **d** is 1.6 nm.

Cr absorption edge at 574 eV. The image of the pattern with 19.5 nm lines and spaces (Fig. 4a) shows good modulation (20%), whereas the image of 15.1 nm lines and spaces (Fig. 4c) shows no modulation with this lens. As seen in Fig. 5, the latter data point is beyond cut-off for the 25 nm lens. Returning to Fig. 4, the two images on the right side, Fig. 4b and d, were obtained with the 15 nm zone plate lens, at a wavelength of 1.52 nm (815 eV). The shorter wavelength allowed us to maintain a convenient working distance. Images obtained with the 15 nm outer zone width lens (Fig. 4b and d) show clear improvements when compared to those with the 25 nm zone plate. The 19.5 nm image in Fig. 4b displays less noise and better contrast than that in Fig. 4a. The improvement is particularly evident in images of the 15.1 nm lines, for which the earlier results with the 25 nm lens showed no modulation (Fig. 4c), whereas the image obtained with the 15 nm lens (Fig. 4d) shows excellent modulation.

An intensity profile ('lineout') of Fig. 4d shows a modulation of 3,000 counts per pixel and a peak level of 40,000 counts per pixel in the CCD image, corresponding to a modulation of approximately 8%. To determine the optical modulation transfer function (MTF) of the system, knowledge of the intrinsic sample contrast is needed. This can be calculated using the known absorption parameters for Si and Cr, and the sample thickness. The sample thickness varies from zero (clear area) to many micrometres. The image was taken near the clear area, where we estimate the sample thickness to be approximately 50 nm (about a 3:1 aspect ratio, which generally provides good images). In this case, at a photon energy of 815 eV, the Si transmits 97% of the photons and the Cr transmits 64%. The image modulation, calculated using SPLAT for an ideal sample with equal 15 nm lines and spaces, is 20% for a perfect lens. Allowing for an imperfect lens with an MTF of 50%, close to its resolution limit, we expect only a 10% CCD image modulation. This value is within the error bars of the observed value. The same analysis applies to the 19.5 nm image in Fig. 4b, where the recorded CCD modulation is about 4,000 photons per pixel on a 36,000 photons per pixel background, or 11%. Unfortunately, because of the uncertainty in the sample thicknesses, and to a lesser extent the presence of somewhat non-uniform stray light, which affects the determination of image modulation, it is not possible unambiguously to assign MTF values on the basis of these two measurements. It is worth noting, however, that modest image modulations with thin, high resolution samples are not unusual, and indeed those observed here are similar to those seen with our previously described 25 nm zone plate, which has been used successfully in many scientific studies.

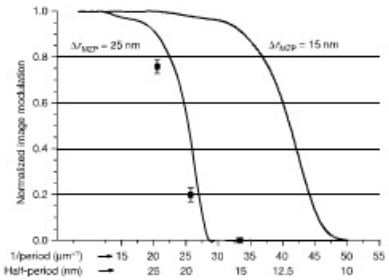

Figure 5 | The calculated modulation transfer functions of the microscope with two different zone plates. One zone plate has an outer zone width, Δr_{MZP} of 25 nm (left line), and the other has Δr_{MZP} = 15 nm (right line). The theoretical resolution for the two lenses are 19 nm and 12 nm, respectively. Also shown are data indicating the degree of modulation obtained for various test patterns using the Δr_{MZP} = 25 nm (squares). The Δr_{MZP} = 25 nm zone plate yielded 75% modulation for a half-period of 24.3 nm, 20% for 19.5 nm, and 0% modulation for a half-period of 15.1 nm (Fig. 4a and c). Values are means ± s.d. Using the Δr_{MZP} = 15 nm zone plate, image quality is much improved, as seen in Fig. 4b and d, but owing to uncertain sample thicknesses and stray light an accurate determination of the modulation was not possible.

Modelling of the MTF for the two lenses is shown by solid lines in Fig. 5. This computational modelling accounts for the partially coherent, hollow-cone, soft X-ray illumination employed in each case. With the higher numerical aperture ($NA = \lambda/2\Delta r$), the simulation predicts a proportionately increased resolving power, as indicated by the MTF shift to higher spatial frequencies. With this degree of partially coherent illumination, we calculate a theoretically achievable resolution of approximately $0.8\Delta r$, or 20 nm with the 25 nm zone plate and 12 nm with the 15 nm zone plate. This is consistent with the images in Fig. 4, and with the three data points in Fig. 5 for the 25 nm lens. Data points for the 15 nm lens (Fig. 4b and d) are not shown in Fig. 5 owing to insufficient knowledge of the sample thickness and the presence of somewhat non-uniform stray light, as mentioned above. We believe that the improved imaging capability, as illustrated in Fig. 4, and supported by Fig. 5, are the clearest demonstration of a significant advance with the present zone plate fabrication technique. In the near future, with the high electron beam placement accuracy and the ability of PMMA to support isolated features as small as 5 nm (ref. 27), we expect our overlay nanofabrication technique to yield high quality zone plates with outer zone widths of 10 nm, permitting a spatial resolution of 8 nm. Additional benefits of this overlay technique will be to permit higher aspect ratio zones for improved efficiency and, separately, the stacking of subzonal structures for additional improvement of efficiency, perhaps in a trade-off for resolution in multilevel zone plates[28].

In addition to improved spatial resolution, which scales as Δr, the zone plates reported here significantly reduce the depth of field, which scales[20] as $(\Delta r)^2$, thus offering a new capability for soft X-ray optical sectioning, and the further potential for improved spatial resolution soft X-ray tomography. This will require further efforts to model soft X-ray propagation through sequential two-dimensional image sections. In the life sciences, when combined with protein specific labelling[5], these advances would permit quantitative protein localization in three-dimensional images of the cell, and thus permit studies of gene expression as a function of mutations, knockout genes, and so on (C. A. Larabell, personal communication).

With the existence of more than 30 synchrotron facilities worldwide, these advances in soft X-ray microscopy could be readily available to the research community. Furthermore, we anticipate that compact soft X-ray sources will also be available in the not too distant future, using laser-produced plasmas[29], femtosecond laser high harmonic techniques[30], or extreme-ultraviolet/soft X-ray lasers[31]. With these advances, we anticipate a wider use of zone plate based soft X-ray microscopy across the broad range of nanoscience and nanotechnology.

Received 3 September 2004; accepted 3 May 2005.

1. Susini, J. & Joyeux, D. & Polack, F. (eds) *X-Ray Microscopy VII* (EDP Sciences, Paris, 2003).
2. Chao, W. *et al.* 20-nm-resolution soft x-ray microscopy demonstrated by use of multilayer test structures. *Opt. Lett.* **28**, 2019–2021 (2003).
3. Kipp, L. *et al.* Sharper images by focusing soft X-rays with photon sieves. *Nature* **414**, 184–188 (2001).
4. Eisebitt, S. *et al.* Lensless imaging of magnetic nanostructure by x-ray spectroholography. *Nature* **432**, 885–888 (2004).
5. Miao, J., Charalambous, P., Kirz, J. & Sayre, D. Extending the methodology of X-ray crystallography to allow imaging of micrometre-sized non-crystalline specimens. *Nature* **400**, 342–344 (1999).
6. Miao, J. W. *et al.* Imaging whole *Escherichia coli* bacteria by using single-particle x-ray diffraction. *Proc. Natl Acad. Sci. USA* **100**, 110–112 (2003).
7. Marchesini, S. *et al.* X-ray image reconstruction from a diffraction pattern alone. *Phys. Rev. B* **68**, 140101–140104 (2003).
8. Meyer-Ilse, W. *et al.* High resolution protein localization using soft x-ray microscopy. *J. Microsc.* **201**, 395–403 (2001).
9. Larabell, C. A. & Le Gros, M. A. X-ray tomography generates 3-D reconstructions of the yeast, *Saccharomyces cerevisiae*, at 60-nm resolution. *Mol. Biol. Cell* **15**, 957–962 (2003); movie at (http://ncxt.LBL.gov/movies/video-seg8.mov).
10. Myneni, S. C. B., Brown, J. T., Martinez, G. A. & Meyer-Ilse, W. Imaging of humic substance macromolecular structures in water and soils. *Science* **286**, 1335–1337 (1999).
11. Juenger, M. C. G., Lamour, V. H. R., Monteiro, P. J. M., Gartner, E. M. & Denbeaux, G. P. Direct observation of cement hydration by soft X-ray transmission microscopy. *J. Mater. Sci. Lett.* **22**, 1335–1337 (2003).
12. Fischer, P., Schutz, G., Schmahl, G., Guttmann, P. & Raasch, D. Imaging of magnetic domains with the X-ray microscope at BESSY using X-ray magnetic circular dichroism. *Z. Phys. B* **101**, 313–316 (1996).
13. Fischer, P. *et al.* Study of magnetic domains by magnetic soft x-ray transmission microscopy. *J. Phys. D* **35**, 2391–2397 (2002).
14. Stoll, H. *et al.* High-resolution imaging of fast magnetization dynamics in magnetic nanostructures. *Appl. Phys. Lett.* **84**, 3328–3330 (2004).
15. Schneider, G. *et al.* Electromigration in passivated Cu interconnects studied by transmission x-ray microscopy. *J. Vac. Sci. Technol. B* **20**, 3089–3094 (2002).
16. Schneider, G. *et al.* Computed tomography of cryogenic cells. *Surf. Rev. Lett.* **9**, 177–183 (2002).
17. Meyer-Ilse, W. *et al.* New high-resolution zone-plate microscope at Beamline 6.1 of the Advanced Light Source. *Synchr. Radiat. News* **8**, 29–33 (1995).
18. Schmahl, G. & Rudolph, D. (eds) *X-ray Microscopy* (Springer, Berlin, 1984).
19. Anderson, E. H. *et al.* Nanofabrication and diffractive optics for high-resolution x-ray applications. *J. Vac. Sci. Technol. B* **18**, 2970–2975 (2000).
20. Attwood, D. T. *Soft X-Rays and Extreme Ultraviolet Radiation* (Cambridge Univ. Press, Cambridge, UK, 2000).
21. Goodman, J. W. *Statistical Optics* 303–324 (Wiley, New York, 2000).
22. Born, M. & Wolf, E. *Principles of Optics* 7th edn, 441, 596–606 (Cambridge Univ. Press, Cambridge, UK, 1999).
23. Toh, K. K. H. & Neureuther, A. R. Identifying and monitoring effects of lens aberrations in projection printing. *Proc. SPIE* **772**, 202–209 (1987).
24. Anderson, E. H., Boegli, V. & Murray, L. P. Electron beam lithography digital pattern generator and electronics for generalized curvilinear structures. *J. Vac. Sci. Technol. B* **13**, 2529–2534 (1995).
25. Anderson, E. H., Ha, D. & Liddle, J. A. Sub-pixel alignment for direct-write electron beam lithography. *Microelectron. Eng.* **73–74**, 74–79 (2004).
26. Chao, W. *et al.* Demonstration of 20 nm half-pitch spatial resolution with soft x-ray microscopy. *J. Vac. Sci. Technol. B* **21**, 3108–3111 (2003).
27. Yasin, S., Hasko, D. G. & Ahmed, H. Fabrication of <5 nm width lines in poly(methylmethacrylate) resist using a water:isopropyl alcohol developer and ultrasonically-assisted development. *Appl. Phys. Lett.* **78**, 2760–2762 (2001).
28. Di Fabrizio, E. *et al.* High-efficiency multilevel zone plates for keV X-rays. *Nature* **401**, 895–898 (1999).
29. Vogt, U. *et al.* High-resolution spatial characterization of laser produced plasmas at soft x-ray wavelengths. *Appl. Phys. B* **78**, 53–58 (2004).
30. Gibson, E. A. *et al.* Coherent soft x-ray generation in the water window with quasi-phase matching. *Science* **302**, 95–98 (2003).
31. Larotonda, M. A. *et al.* Characteristics of a saturated 18.9 nm table top laser operating at 5 Hz repetition rate. *IEEE J. Select. Topics Quant. Electron.* **10**, 1363–1367 (2004).

Acknowledgements The authors acknowledge financial support from the National Science Foundation's Engineering Research Centre Program, the Department of Energy's Office of Science, Office of Basic Energy Sciences, and the Defense Advanced Research Projects Agency.

Author Information Reprints and permissions information is available at npg.nature.com/reprintsandpermissions. The authors declare no competing financial interests. Correspondence and requests for materials should be addressed to W.C. (wichao@lbl.gov).